NANOMATERIALS

Building two-dimensional materials one row at a time: Avoiding the nucleation barrier

Jiajun Chen[1,2], Enbo Zhu[3,4], Juan Liu[5], Shuai Zhang[2], Zhaoyang Lin[6], Xiangfeng Duan[6,7], Hendrik Heinz[5], Yu Huang[3,7]*, James J. De Yoreo[1,2]*

Assembly of two-dimensional (2D) molecular arrays on surfaces produces a wide range of architectural motifs exhibiting unique properties, but little attention has been given to the mechanism by which they nucleate. Using peptides selected for their binding affinity to molybdenum disulfide, we investigated nucleation of 2D arrays by molecularly resolved in situ atomic force microscopy and compared our results to molecular dynamics simulations. The arrays assembled one row at a time, and the nuclei were ordered from the earliest stages and formed without a free energy barrier or a critical size. The results verify long-standing but unproven predictions of classical nucleation theory in one dimension while revealing key interactions underlying 2D assembly.

Assembly of two-dimensional (2D) molecular arrays on surfaces has been extensively investigated to understand the structural relation between substrate and film (*1*–*6*), revealing a rich world of frameworks (*1*, *2*, *6*), tilings (*1*, *7*), and chiral architectures (*1*, *8*). Recognition of the electronic (*9*), optical (*9*), chemical (*2*–*4*), and mechanical (*10*) properties of 2D materials has intensified interest in their formation, yet little attention has been given to the underlying mechanism. Whether assembly is described by concepts of classical nucleation theory (CNT) (*11*) or falls within the broader context of "nonclassical" pathways involving formation, aggregation, and transformation of transient precursors (*12*) remains unknown. Using peptides chosen by genetic selection (*13*, *14*) for their binding affinity to MoS_2 (0001), we investigated nucleation of 2D arrays by molecularly resolved in situ atomic force microscopy (AFM) and molecular dynamics (MD) simulations.

The peptides consisted of seven amino acids [Tyr-Ser-Ala-Thr-Phe-Thr-Tyr (YSATFTY), named MoSBP1] with acylated and amidated N and C termini, respectively, to reduce electrostatic interactions (*15*) (fig. S1). When incubated with freshly cleaved MoS_2 substrates, MoSBP1 assembled into elongated islands aligned along three equivalent directions on MoS_2 (0001) and exhibited aspect ratios that decreased with increasing peptide concentration (Fig. 1, A to C). The islands were ~0.7 nm in height (fig. S2), indicating that they were one monolayer thick, and consisted of parallel rows with a periodicity of 4.1 nm (Fig. 1, D to F, and fig. S3). Comparison of the row directions to the underlying MoS_2 (0001) lattice demonstrated that they formed at an angle of 30° to the densest sulfur packing directions (fig. S4).

Molecular-resolution imaging showed that each row consists of ~1.1 nm × 4.7 nm units running at ~60° to the rows (Fig. 1, E and F), demonstrating the highly ordered structure of each row (Fig. 1F and fig. S5). The dimensions and symmetry of the units were consistent with dimer formation with the same termini of the two monomers facing one another (C-to-C or N-to-N), as indicated by the following observations: (i) The length of each unit was ~1.7 times the maximum possible length of a fully extended MoSBP1 molecule. (ii) The units exhibited two-fold symmetry down to a submolecular level. (iii) The central portion of each unit was higher than the ends, suggesting overlap of the peptides in that region. (iv) The absence of chains extending along the direction parallel to the dimers, which would result in variable row widths, excluded an N-to-C or C-to-N association within the dimers. (v) Ring-like structures ~0.5 nm in diameter, similar to the size reported in other AFM studies of a flat-lying phenyl ring (*16*), lay symmetrically on both sides of the rows (fig. S5C).

To understand the detailed structure and key interactions that stabilized the film, we performed MD simulations using the CHARMM-Interface force field (*17*) starting with single

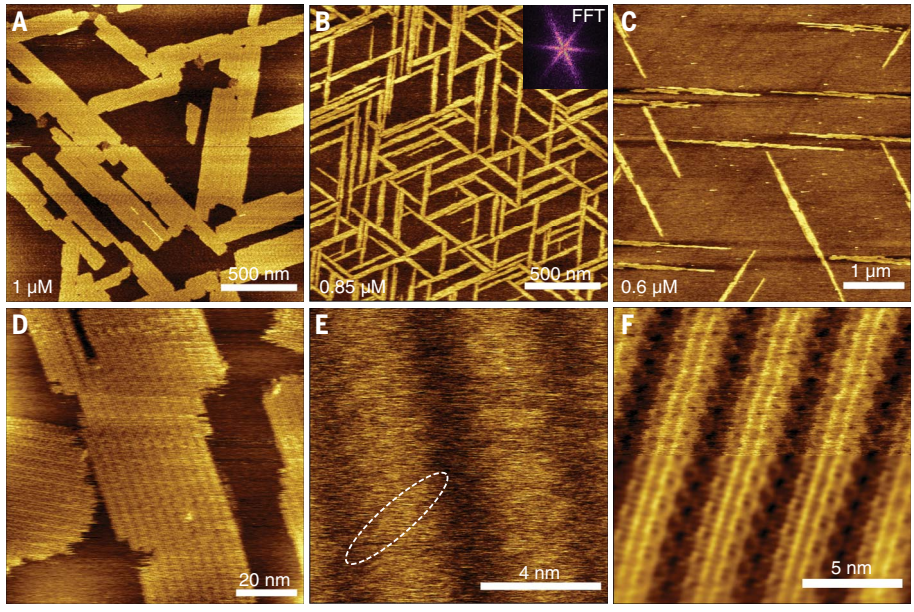

Fig. 1. In situ AFM images of MoSBP1 on MoS_2 (0001). (**A** to **C**) Self-assembled structure at different concentrations. (**D**) Islands consist of co-aligned rows with uniform spacing. (**E**) Non–contact mode image shows that each row consists of small building blocks lying at ~60° to the row orientation. (**F**) High-resolution contact mode image shows detailed structure with connections between rows. The bottom half of (F) was fast Fourier transform–filtered.

[1]Department of Materials Science and Engineering, University of Washington, Seattle, WA 98195, USA. [2]Physical Sciences Division, Pacific Northwest National Laboratory, Richland, WA 99352, USA. [3]Department of Materials Science and Engineering, University of California, Los Angeles, CA 90095, USA. [4]School of Materials Science and Engineering, Beijing Institute of Technology, Beijing 100081, P. R. China. [5]Department of Chemical and Biological Engineering, University of Colorado, Boulder, CO 80309, USA. [6]Department of Chemistry and Biochemistry, University of California, Los Angeles, CA 90095, USA. [7]California NanoSystems Institute, University of California, Los Angeles, CA 90095, USA.
*Corresponding author. Email: james.deyoreo@pnnl.gov (J.J.D.Y.); yhuang@seas.ucla.edu (Y.H.)

peptides in different orientations on MoS_2 (Fig. 2, A to D). The MoSBP1 binding energy E_{ads} was −96 ± 9 kcal/mol in the preferred orientation (Fig. 2A) and originated from the replacement of ~25 water molecules in direct contact with MoS_2 surface; these were weakly bound and gained more hydrogen bonds upon release into the solution (fig. S6, A to C). The entropy gain of water was partially compensated by entropy loss of the peptide upon binding, as shown on similar surfaces (*18*), and the free energy of adsorption was approximately −103 ± 10 kcal/mol (see supplementary text). We tested all possible peptide orientations, without constraints in any direction, and found that the backbone preferred to align in the densest sulfur packing direction (Fig. 2, A to D). Defining the direction of a single peptide as the orientation perpendicular to the main body of the peptide, we found a strong preference for single peptides to align at 30°, 90°, and 150° relative to the [2$\bar{1}\bar{1}$0] direction of the MoS_2 lattice (Fig. 2, B to E), matching the observed row directions.

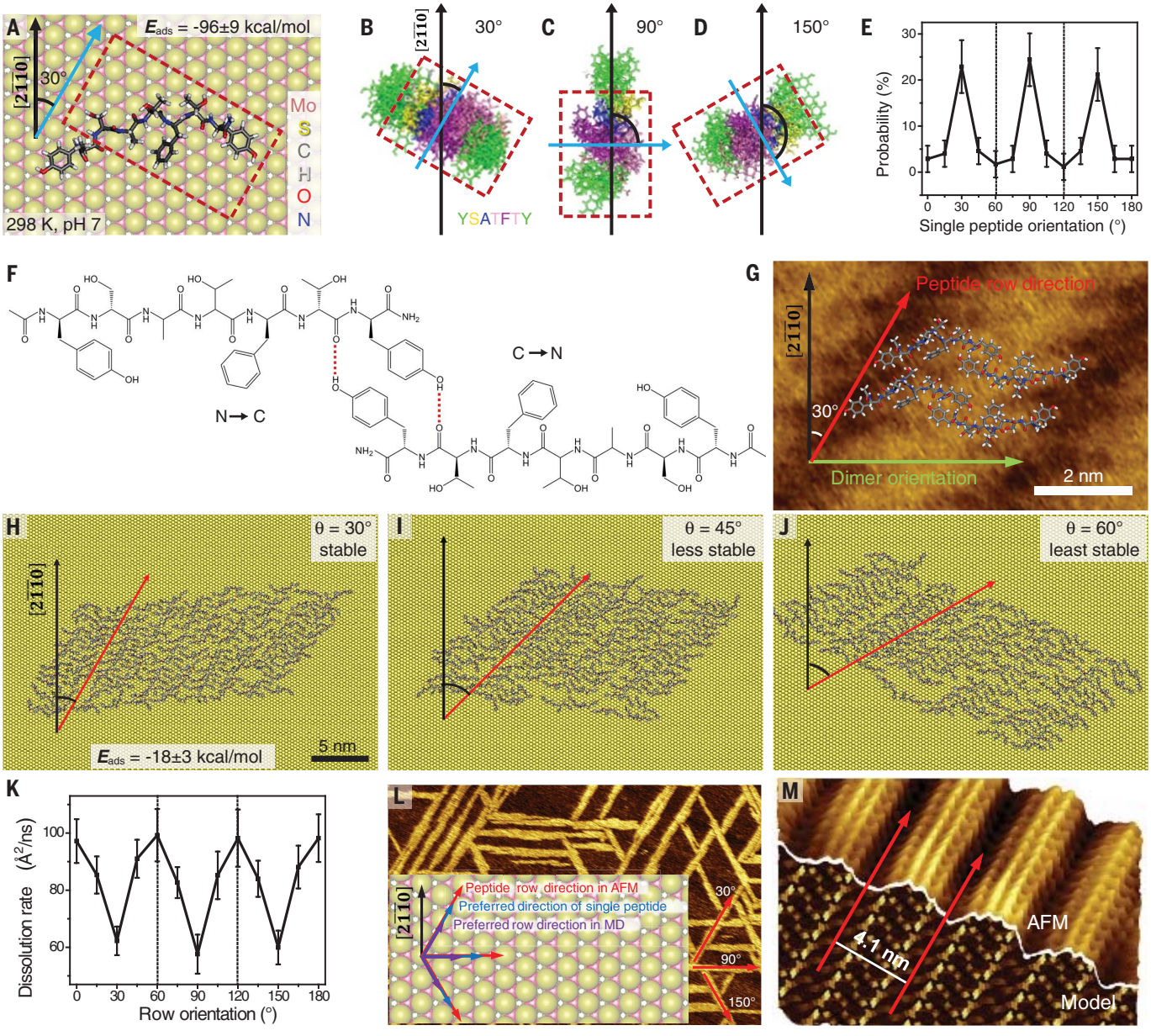

Fig. 2. Predicted alignments of MoSBP1, dimers, and assemblies on MoS_2 (0001) from MD simulations. (**A**) Favorable binding conformation of a single peptide. (**B** to **D**) Preferred orientations of single peptides on the surface, colored by residue (A, Ala; F, Phe; S, Ser; T, Thr; Y, Tyr). Red boxes and blue arrows in (A) to (D) show main body and direction of a single peptide. (**E**) The probability of a single peptide at different angles relative to the [2$\bar{1}\bar{1}$0] direction. (**F**) Proposed dimer arrangement stabilized by hydrogen bonds. (**G**) The most stable dimer conformation, overlaid on an AFM image. The dimer direction points from a phenyl ring at one end of the dimer to another phenyl ring at the other end, which shows a 60° difference from the row direction. (**H** to **J**) Snapshots of ~20-nm peptide assemblies with the dimer arrangement in (G) at different orientations on the surface. (**K**) The stability is highest, and the dissolution rate is lowest, at angles of 30°, 90°, and 150°. (**L**) Preferred orientations from MD agree with experimental results. (**M**) Simulated AFM image of peptide rows along the preferred orientation is consistent with AFM data. Error bars in (E) and (K) denote SD in the simulation.

To understand the stabilization of peptide rows, we simulated numerous dimer configurations, the most stable of which is shown schematically in Fig. 2F and overlaid on an AFM image in Fig. 2G. We tested the stability of large assemblies of these dimers ~20 nm in size with different row orientations relative to the lattice in MD simulations (Fig. 2, H to J). Peptide row stability was again substantially higher when aligned at 30°, 90°, and 150° relative to $[2\bar{1}\bar{1}0]$ (Fig. 2, K and L). In all cases, some disorder was introduced during the simulation, presumably because of the smaller domain size relative to experiments and some limitations in both conformation sampling and force fields.

The most stable structures (Fig. 2, H and K) were consistent with the topography seen by AFM (Fig. 2, L and M); a simulated AFM image based on the MD results (Fig. 2M) confirmed the importance of the phenyl rings of Tyr and Phe in surface recognition and attachment (fig. S6, A to C). The dimer itself was stabilized by hydrogen bonds between the –OH of Tyr[7] and the –C=O of Thr[6], and possibly by π-π stacking between phenyl rings (Fig. 2F). Interestingly, the adsorption of multiple peptides in large assemblies reduced the attraction per peptide from –96 to –18 kcal/mol (Fig. 2, A and H). Although this energy still corresponded to strong binding (fig. S6, E and F), this result indicated that the required removal of 25 water molecules to bind a single peptide was kinetically prohibited and that the ordered domains of dimer rows represented a metastable state, which was more rapidly achieved

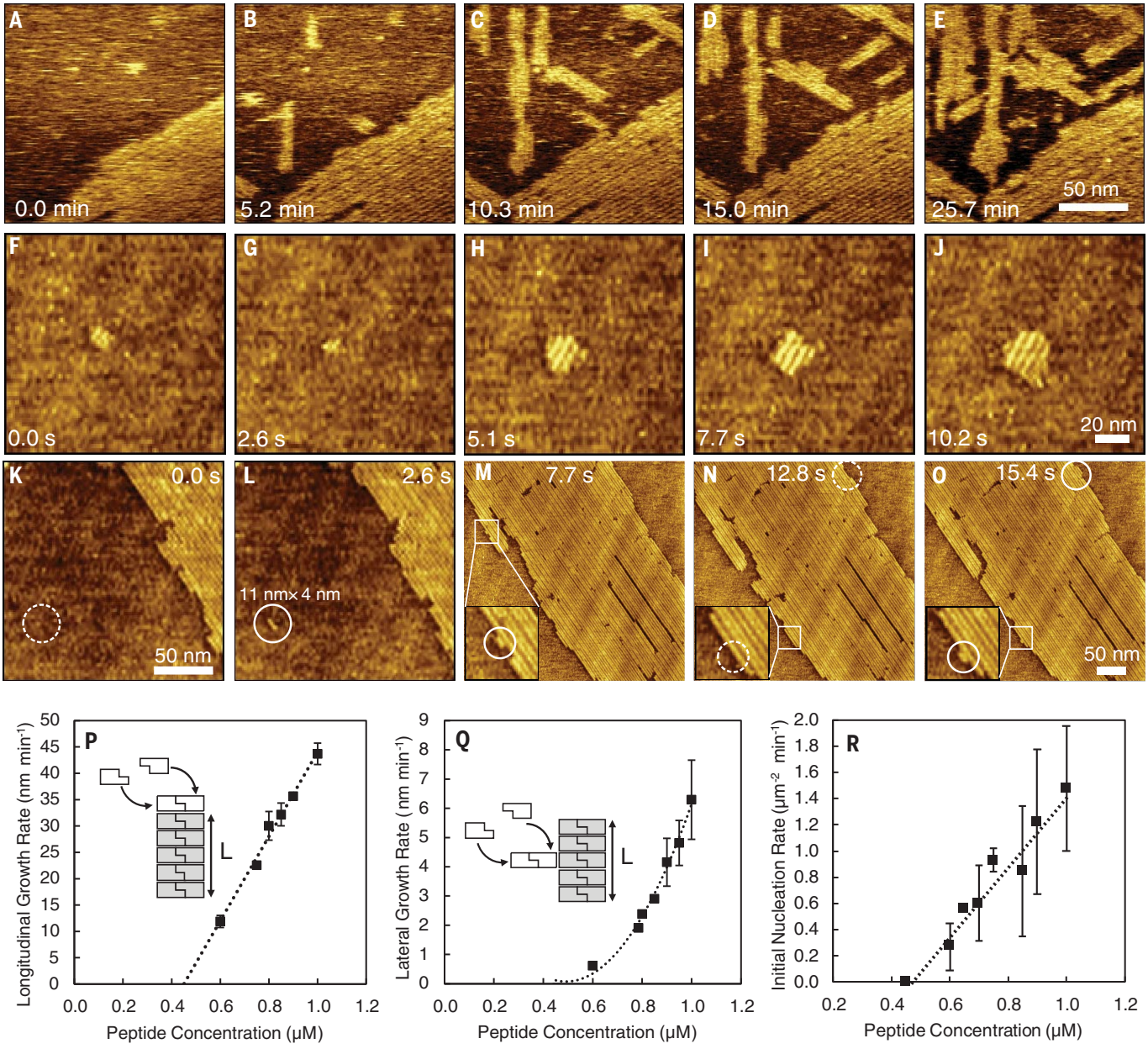

Fig. 3. Nucleation and growth dynamics of MoSBP1 on MoS_2 (0001). (**A** to **E**) In situ AFM images show that the peptides attached to the surface and directly grew into ordered structures. (**F** to **O**) In situ high-speed AFM images show formation and development of a small island [(F) to (J)]; nucleation of a single row [(K) and (L)]; and creation of new rows adjacent to existing ones [(M) to (O)]. Circles highlight regions where new rows appear (dashed, before; solid, after). (**P** to **R**) Longitudinal (P) and lateral (Q) island growth rates and initial nucleation rate (R) versus peptide concentration.

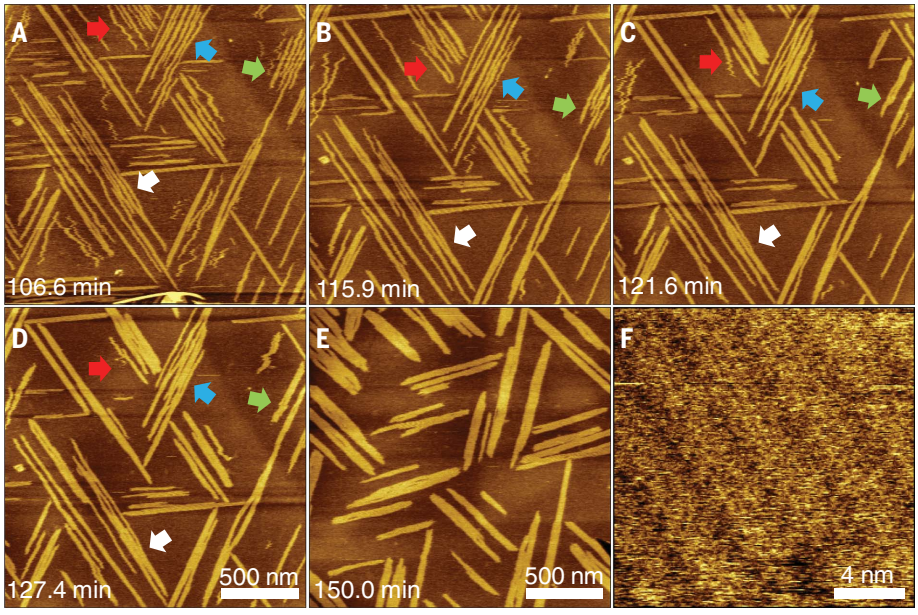

Fig. 4. In situ AFM images of MoSBP1 on HOPG. (**A** to **D**) Sequence of images showing that rows of MoSBP1 on HOPG can diffuse across the surface (arrows), aggregating with other rows to form immobile islands. (**E**) Aggregated islands at another location show the final state of these single rows as constituents of compact 2D islands. (**F**) High-resolution image shows the highly ordered structure of these islands.

via hydrogen bonding and van der Waals interactions.

We further investigated the pathway and kinetics of array formation by continuously monitoring assembly by AFM, with scan rates as high as 2.56 s per frame (Fig. 3, A to O, fig. S7, and movie S1). The results showed that MoSBP1 nuclei exhibited the elongated structure of mature islands and grew along the preferred lattice directions from their first appearance, with no evidence of a transient precursor phase or attachment of large clusters over the course of ~900 sequential frames, according to our current time resolution (Fig. 3, F to O, fig. S7, and movie S1). Moreover, the characteristic 4.1-nm rows aligned along one of the three preferred directions were observed even in the smallest islands with lengths as short as ~8 dimers (~9 nm) (Fig. 3, G and L), further indicating a direct nucleation pathway. Simulation of single peptides and circular dichroism spectra showed that MoSBP1 tended to remain in a monomeric state in bulk solution, which suggests that monomers were the likely growth unit (see supplementary text).

In the early stages of assembly, a few islands grew along directions lying at 30° to the preferred directions, but disappeared over time (~25 min) (fig. S8). Islands that grew along the preferred directions sometimes dissolved as nearby islands grew (~10 min) (fig. S9). These observations demonstrated both the higher stability of islands exhibiting dominant orientations and the reversibility of peptide binding (movie S1).

To understand the energetic controls on assembly, we used time-resolved in situ data to measure nucleation and growth rates, which revealed the crucial role of row-by-row assembly in controlling film formation. The longitudinal growth rate v_{lg} was proportional to peptide concentration c (Fig. 3P), whereas the lateral growth rate v_{la} was proportional to c^2 (Fig. 3Q). The initial nucleation rate J_n was also proportional to c (Fig. 3R), as was the number density of nuclei n_∞ approached asymptotically as time $t \rightarrow \infty$ (fig. S10). Moreover, the concentration below which $J_n = 0$ (0.48 μM), within error, was identical to that at which v_{lg} and v_{la} reached zero (0.45 μM)—that is, the island solubility limit c_e—and there was no lower limit to the size of nuclei that grew spontaneously (fig. S11). Thus, nucleation began as soon as c exceeded c_e, $J_n \propto c$, and the critical island size $N_c = 0$.

These observations are seemingly in violation of predictions of CNT, which hold that 2D islands exhibit a critical size below and above which islands will, on average, dissolve and grow, respectively, and that N_c should scale inversely with supersaturation σ. Moreover, in two dimensions, CNT predicts an exponential dependence of J_n on σ, leading to a strongly nonlinear dependence on c (*11*, *19*). We can reconcile the apparent contradictions and understand all of the observed phenomena by recognizing that, although the final islands are 2D, they form one row at a time. The free energy barrier of CNT arises from the difference in the dimensional dependence between the free energy change ΔG associated with the drop in chemical potential upon crystallization and that associated with surface (3D) or line (2D) tension of the new phase. In two dimensions, the (negative) first term scales with island area A, whereas the (positive) second term is proportional to the perimeter. The second term dominates at small size, but the first term eventually wins out, giving rise to a barrier at finite A and a critical size N_c (*11*, *19*) (fig. S12). In contrast, in one dimension, both contributions to ΔG are proportional to the length L of the nucleus; consequently, there is no barrier, and $N_c = 0$ (fig. S12). Thus, when the assembly process is viewed as continual nucleation of 1D rows, rather than conflicting with CNT, the results verify its long-standing prediction that nucleation of 1D structures occurs without a free energy barrier.

The distinction between the nucleation kinetics of MoSBP1 rows and that of amyloid fibrils, which constitute a quasi-1D material, further highlights the 1D nature of MoSBP1 nucleation. In the amyloid fibril system, which exhibits similar 1D growth behavior, a two-step condensation-ordering process with a nucleation barrier is widely observed (*20*). However, in that system, the initial formation of the disordered oligomeric precursor phase constitutes the nucleation step and leads to the typical shape of the nucleation barrier in three dimensions as described by CNT (*20*).

The fact that there is no free energy barrier to nucleation does not mean that nucleation occurs in the absence of density fluctuations, which all systems at finite temperature must possess. However, when building 1D structures, even density fluctuations that create dimers create supercritical nuclei, because the monomer defines the critical cluster size. The lack of a free energy barrier also does not mean that nucleation—or, for that matter, growth—is unopposed by kinetic barriers associated with molecular-level processes, such as desolvation, conformational changes, or breaking and making of hydrogen bonds. However, these activation barriers are fundamentally different from free energy barriers that are associated with the ability of the system to explore all the available configurational states and are governed by the probability of forming an island larger than the critical size. The activation barriers do not depend on supersaturation and thus have no impact on the dependence of J_n on σ. However, because J_n depends exponentially on both the free energy barrier and the activation barrier, both are important in determining the frequency of nucleation. Thus, even though the lack of a free energy barrier leads to a linear dependence of rate on concentration, the finite activation barrier ensures that nucleation occurs nonetheless through discrete events.

The difference in the concentration dependence of longitudinal and lateral growth rates can also be understood as a consequence of row-by-row growth. Monomers that attach at the row ends are strongly bound, and every attachment is an independent event. Thus, v_{lg} should be linear in c, as observed (Fig. 3P). However, when a new row ($n = 2$) forms adjacent to the first ($n = 1$), the weakness of end-to-end binding causes the attached monomers to have low stability, such that

the creation of a stable dimer requires a second attachment event before the first monomer detaches (Fig. 3Q). Hence, v_{1a} should be quadratic in c. This difference explains why increasing c leads to smaller island aspect ratios (Fig. 1, A to C): The rate at which rows $n \geq 2$ are created relative to the rate at which existing rows lengthen is proportional to $(c - c_e)$. In addition, the fact that the lateral growth rate also reaches zero at $c = c_e$ further demonstrates the barrier-free nature of nucleation in this system. The lateral growth rate is directly proportional to the rate at which new rows nucleate heterogeneously along existing rows. Although this rate can be expected to exceed that of new, isolated rows (i.e., homogeneous nucleation), in CNT the kinetics of heterogeneous nucleation are governed by the same expressions with a modified value of the surface or line tension. Thus, a critical size and barrier would be expected for 2D nuclei.

The question then arises as to why the nucleation rate of the first row is linear in c, whereas that of rows $n \geq 2$ is quadratic. We constructed a set of rate equations to describe the creation and destruction of all adsorbed species, including monomers, dimers, and rows (see supplementary text), and derived the initial nucleation rate dn/dt (near $t = 0$):

$$\frac{dn}{dt} \approx \frac{k_m^+ k_n^+ c^2}{c(k_m^+ + k_n^+) + k_m^-} - \frac{k_m^+ k_n^+ c_e^2}{c_e(k_m^+ + k_n^+) + k_m^-} \quad (1)$$

where k_m^+, k_n^+, and k_m^- are the rate coefficients for monomer adsorption, attachment to an adsorbed monomer to form a nucleus, and desorption, respectively. In the limit of high k_m^- (i.e., low coverage), $J_n \propto c^2$. However, at high k_m^+—high monomer coverage—$J_n \propto c$, because every adsorbing monomer has a high probability of finding a monomer that has already adsorbed. Thus, although the need to dock a monomer to the side of a row leads to a quadratic dependence on c for nucleation of rows $n \geq 2$, a high coverage of adsorbed monomers produces a linear dependence on c for the first row of any island.

Finally, to determine the impact of sequence and surface on the pathway, we investigated assembly on MoS_2 (0001) by three other sequences—the reversed sequence MoSBP1-R (Tyr-Thr-Phe-Thr-Ala-Ser-Tyr; YTFTASY), the scrambled sequence MoSBP1-S (Ser-Ala-Tyr-Phe-Tyr-Thr-Thr; SAYFYTT), and a weak-binding sequence, MoSBP20 (Thr-Ser-His-Met-Ser-Asn-Thr; TSHMSNT)—as well as assembly of the original sequence on highly ordered pyrolytic graphite (HOPG). The reversed sequence MoSBP1-R assembled on MoS_2 into a structure similar to that of MoSBP1 (fig. S13, A to C), although a larger concentration (5 μM) was required to initiate nucleation and growth. For both the scrambled version MoSBP1-S, which still contained the phenyl rings, and the weak-binding sequence MoSBP20, which contained no phenyl rings, no assembly occurred (fig. S13, D and E) even at $c = 5$ μM.

Substitution of HOPG for MoS_2 revealed yet another assembly pathway made possible through the row-by-row nucleation process. MoSBP1 still assembled into 2D films similar to those seen on MoS_2 (Fig. 4), but most of the rows constituting these films began as isolated independent nuclei (Fig. 4, A to D). Over time, the MoSBP1 rows, which were immobile on MoS_2, were able to diffuse across the HOPG surface and aggregate to form the final compact, highly ordered 2D domains (Fig. 4, E and F). Individual rows aligned along metastable orientations were more mobile, aiding in the aggregation process (fig. S14). These results highlight the key role of epitaxial match in tuning the assembly pathway. Although MoSBP1 exhibits commensurate epitaxial growth on MoS_2, the mismatch with the HOPG lattice leads to strained epitaxy (fig. S14). The effect of this strain is revealed through the smaller row spacing of 3.4 nm on HOPG versus 4.1 nm on MoS_2 and weaker binding, which leads to the observed mobility of the rows.

The use of peptides identified through phage display (*13*–*15*) has enabled control over the formation of a wide range of materials (*13*–*15*, *21*–*24*), and surface-directed assembly of such peptides has been shown to modulate the electronic properties of 2D materials (*25*). In cases where structure has been investigated, patterns like those observed here are commonly reported. Our findings provide a mechanistic description of their formation and define the key controlling parameters.

The peptides investigated here exhibit structural features common to many polymeric and chain-like organic molecules that self-assemble on surfaces (*2*–*5*, *8*, *21*, *25*, *26*): They possess a mix of hydrophobic and hydrophilic groups; they form many contacts between side chains and with both neighboring molecules and the underlying substrate; and, relative to side-to-side binding, they exhibit weak end-to-end binding. Indeed, a wide variety of systems form ordered 2D films exhibiting a row-by-row structure (*21*, *25*–*28*). In addition, many peptides and other polymers form 1D fibers in bulk solution that then interact to form 2D and 3D structures (*29*–*32*). The above findings place these systems in the context of well-developed theories for the emergence of order and post-nucleation growth and provide a guide for interpreting and controlling their assembly.

REFERENCES AND NOTES

1. J. V. Barth, G. Costantini, K. Kern, *Nature* **437**, 671–679 (2005).
2. J. A. Elemans, S. Lei, S. De Feyter, *Angew. Chem. Int. Ed.* **48**, 7298–7332 (2009).
3. J. C. Love, L. A. Estroff, J. K. Kriebel, R. G. Nuzzo, G. M. Whitesides, *Chem. Rev.* **105**, 1103–1169 (2005).
4. F. Rosei *et al*., *Science* **296**, 328–331 (2002).
5. J. A. Theobald, N. S. Oxtoby, M. A. Phillips, N. R. Champness, P. H. Beton, *Nature* **424**, 1029–1031 (2003).
6. X. Y. Wang, A. Narita, K. Müllen, *Nat. Rev. Chem.* **2**, 0100 (2017).
7. S. Whitelam, I. Tamblyn, J. P. Garrahan, P. H. Beton, *Phys. Rev. Lett.* **114**, 115702 (2015).
8. M. Lingenfelder *et al*., *Angew. Chem. Int. Ed.* **46**, 4492–4495 (2007).
9. A. K. Geim, I. V. Grigorieva, *Nature* **499**, 419–425 (2013).
10. Y. Suzuki *et al*., *Nature* **533**, 369–373 (2016).
11. D. Kashchiev, *Nucleation: Basic Theory with Applications* (Butterworth-Heinemann, 2000).
12. J. J. De Yoreo *et al*., *Science* **349**, aaa6760 (2015).
13. M. Sarikaya, C. Tamerler, A. K. Y. Jen, K. Schulten, F. Baneyx, *Nat. Mater.* **2**, 577–585 (2003).
14. S. R. Whaley, D. S. English, E. L. Hu, P. F. Barbara, A. M. Belcher, *Nature* **405**, 665–668 (2000).
15. C. Y. Chiu *et al*., *Nat. Chem.* **3**, 393–399 (2011).
16. L. Gross *et al*., *Nat. Chem.* **2**, 821–825 (2010).
17. H. Heinz, T. J. Lin, R. K. Mishra, F. S. Emami, *Langmuir* **29**, 1754–1765 (2013).
18. F. S. Emami *et al*., *Chem. Mater.* **26**, 5725–5734 (2014).
19. J. J. De Yoreo, P. G. Vekilov, *Rev. Mineral. Geochem.* **54**, 57–93 (2003).
20. S. Auer, C. M. Dobson, M. Vendruscolo, *HFSP J.* **1**, 137–146 (2007).
21. C. R. So *et al*., *ACS Nano* **6**, 1648–1656 (2012).
22. M. Umetsu *et al*., *Adv. Mater.* **17**, 2571–2575 (2005).
23. W. J. Chung, K. Y. Kwon, J. Song, S. W. Lee, *Langmuir* **27**, 7620–7628 (2011).
24. R. R. Naik, L. L. Brott, S. J. Clarson, M. O. Stone, *J. Nanosci. Nanotechnol.* **2**, 95–100 (2002).
25. Y. Hayamizu *et al*., *Sci. Rep.* **6**, 33778 (2016).
26. M. Nalbach *et al*., *J. Phys. Chem. C* **121**, 24144–24151 (2017).
27. C. Fu *et al*., *Chem. Mater.* **28**, 951–961 (2016).
28. L. Liu *et al*., *Adv. Sci.* **3**, 1500369 (2016).
29. A. T. Haedler *et al*., *J. Am. Chem. Soc.* **138**, 10539–10545 (2016).
30. J. D. Hartgerink, E. Beniash, S. I. Stupp, *Science* **294**, 1684–1688 (2001).
31. H. K. Murnen, A. M. Rosales, J. N. Jaworski, R. A. Segalman, R. N. Zuckermann, *J. Am. Chem. Soc.* **132**, 16112–16119 (2010).
32. L. E. O'Leary, J. A. Fallas, E. L. Bakota, M. K. Kang, J. D. Hartgerink, *Nat. Chem.* **3**, 821–828 (2011).

ACKNOWLEDGMENTS

In situ AFM and analysis were performed at the Pacific Northwest National Laboratory, operated by Battelle for the U.S. Department of Energy (DOE) under contract DE-AC05-76RL01830. **Funding:** Supported by the NSF EFRI 2DARE Program (NSF EFRI-1433541), the NSF CBET program (NSF 1530790), and the NSF DMREF program (NSF 1623947). Simulations were performed using the Argonne Leadership Computing Facility, which is a DOE Office of Science User Facility supported under contract DE-AC02-06CH11357, and the Janus supercomputer at the University of Colorado–Boulder, which is supported by NSF through award CNS-0821794. **Author contributions:** J.C. performed the in situ AFM and high-speed AFM experiments and data analysis, developed the kinetic model, and wrote the manuscript; E.Z. designed and synthesized the peptides; J.L. performed MD simulations and wrote the manuscript; S.Z. performed the high-speed AFM experiments; Z.L. and X.D. provided MoS_2 substrates for peptide selection; H.H. designed the simulations and wrote the manuscript; Y.H. designed the study and the peptides and wrote the manuscript; and J.J.D.Y. designed the study, developed the kinetic model, performed data analysis, and wrote the manuscript. **Competing interests:** The authors declare no competing financial interests. **Data and materials availability:** All data are available in the main text or the supplementary materials.

SUPPLEMENTARY MATERIALS

www.sciencemag.org/content/362/6419/1135/suppl/DC1
Materials and Methods
Supplementary Text
Figs. S1 to S14
Tables S1 and S2
Movie S1
References (*33*–*41*)

8 June 2018; accepted 15 October 2018
10.1126/science.aau4146

Science

Building two-dimensional materials one row at a time: Avoiding the nucleation barrier

Jiajun Chen, Enbo Zhu, Juan Liu, Shuai Zhang, Zhaoyang Lin, Xiangfeng Duan, Hendrik Heinz, Yu Huang and James J. De Yoreo

Science **362** (6419), 1135-1139.
DOI: 10.1126/science.aau4146

No barriers to growing a row

Classical nucleation theory predicts that two-dimensional islands on a surface must reach a critical size before they continue to grow; below that size, they dissolve. Chen *et al.* used phage display to select for short peptides that would bind to molybdenum disulfide (MoS_2) (see the Perspective by Kahr and Ward). Hexagonal arrays of these peptides grew epitaxially as dimers but without a size barrier—the critical nuclei size was zero. Although two-dimensional arrays formed, growth occurred one row at time. Classical nucleation theory indeed predicts the absence of a barrier for such one-dimensional growth.

Science, this issue p. 1135; see also p. 1111